JACS
JOURNAL OF THE AMERICAN CHEMICAL SOCIETY
pubs.acs.org/JACS
Article

Lignin-Supported Heterogeneous Photocatalyst for the Direct Generation of H_2O_2 from Seawater

Aswin Gopakumar, Peng Ren, Jianhong Chen, Bruno Vinicius Manzolli Rodrigues, H. Y. Vincent Ching, Aleksander Jaworski, Sabine Van Doorslaer, Anna Rokicińska, Piotr Kuśtrowski, Giovanni Barcaro, Susanna Monti, Adam Slabon,* and Shoubhik Das*

Cite This: https://doi.org/10.1021/jacs.1c10786
Read Online
ACCESS | Metrics & More | Article Recommendations | Supporting Information

ABSTRACT: The development of smart and sustainable photocatalysts is in high priority for the synthesis of H_2O_2 because the global demand for H_2O_2 is sharply rising. Currently, the global market share for H_2O_2 is around 4 billion US$ and is expected to grow by about 5.2 billion US$ by 2026. Traditional synthesis of H_2O_2 via the anthraquinone method is associated with the generation of substantial chemical waste as well as the requirement of a high energy input. In this respect, the oxidative transformation of pure water is a sustainable solution to meet the global demand. In fact, several photocatalysts have been developed to achieve this chemistry. However, 97% of the water on our planet is seawater, and it contains 3.0−5.0% of salts. The presence of salts in water deactivates the existing photocatalysts, and therefore, the existing photocatalysts have rarely shown reactivity toward seawater. Considering this, a sustainable heterogeneous photocatalyst, derived from hydrolysis lignin, has been developed, showing an excellent reactivity toward generating H_2O_2 directly from seawater under air. In fact, in the presence of this catalyst, we have been able to achieve 4085 μM of H_2O_2. Expediently, the catalyst has shown longer durability and can be recycled more than five times to generate H_2O_2 from seawater. Finally, full characterizations of this smart photocatalyst and a detailed mechanism have been proposed on the basis of the experimental evidence and multiscale/level calculations.

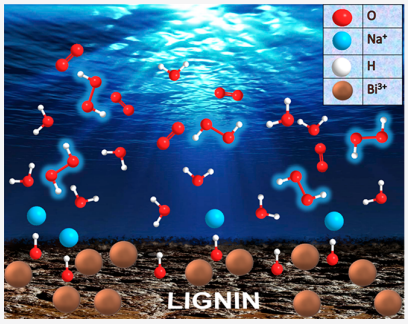

INTRODUCTION

H_2O_2 is a quintessential high-energy oxidant that is widely used in chemical synthesis, mining, environmental remediation, pulp and paper processing, and surfactants.[1] Parallel to these, high energy capacity, easier storage, and transportation make H_2O_2 much more favorable than other conventional green fuels such as H_2.[1] Although relentless efforts have been paid for the generation of H_2 from water, the storage problem of H_2 is still the major bottleneck. Indeed, the energy density of H_2 by volume at atmospheric pressure is far from the practical aspect for stationary fuel storage.[2] To alleviate this storage issue, H_2 must be either physically or chemically captured. However, this step requires external equipment or chemicals, and that increases the associated cost. In this respect, the energy density of aqueous H_2O_2 (70 wt %) is 3.1 MJ L^{-1}, which is very similar (2.8 MJ L^{-1}) to the tank of H_2 at 35 MPa (room temperature) when operating in the fuel cell.[3] Expediently, H_2O_2 has the unique character of being both oxidized and reduced at different electrochemical potentials. That gives an intrinsic facility of using it as a fuel and an oxidant in the fuel cell with a maximum theoretical potential of 1.09 V (Scheme 1).[4] Therefore, it is evident that the demand for H_2O_2 will increase, and as of 2020, the global market share for H_2O_2 is around 4 billion US$ and is expected to grow about 5.2 billion US$ in 2026.[5] Indeed, H_2O_2 has been listed as one of the 100 essential chemicals on the earth.[6]

Scheme 1. Oxidation and Reduction of H_2O_2 at Different Electrochemical Potentials in the Fuel Cell

Anode: $H_2O_2 \rightarrow O_2 + 2H^+ + 2e^-$	+0.68 V *vs.* NHE
Cathode: $H_2O_2 + 2H^+ + 2e^- \rightarrow 2H_2O$	+1.76 V *vs.* NHE
Overall: $2H_2O_2 \rightarrow O_2 + 2H_2O$	1.09 V

Traditionally, H_2O_2 is synthesized by using the anthraquinone method via consecutive hydrogenation and oxidation reactions.[7] This synthetic strategy is associated with high energy input and large quantities of wastewater and solid waste. Thus, a direct combination of H_2 and O_2 to generate H_2O_2 is ideal to avoid all these problems.[1c,7] The mixture of H_2 and O_2 is inevitably associated with high explosion risk and should be very carefully dealt with. Thus, a sustainable strategy

Received: October 12, 2021

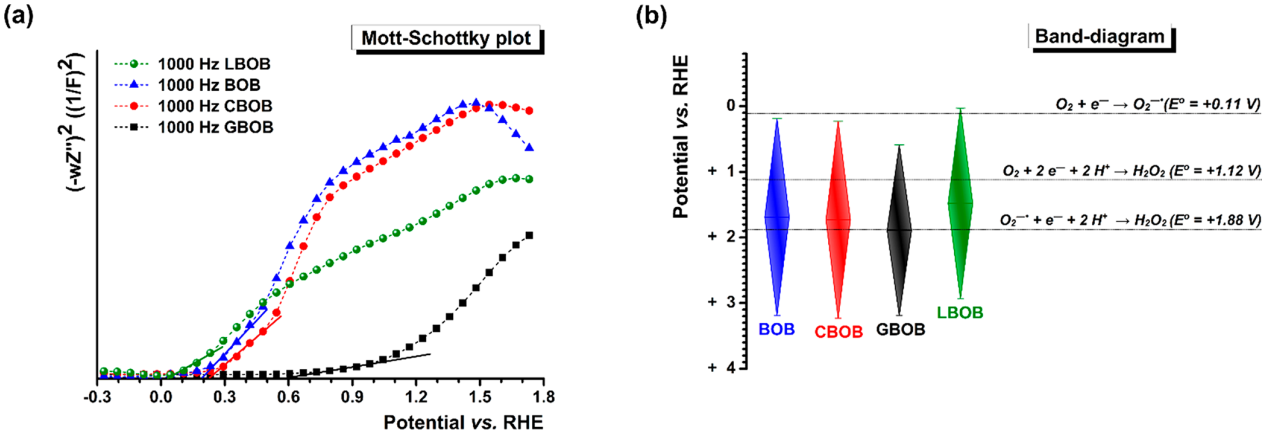

Figure 1. (a) Mott–Schottky plots of the BiOBr catalysts [BiOBr (BOB), chitosan-supported BiOBr (CBOB), graphene-supported BiOBr (GBOB), and lignin-supported BiOBr (LBOB)] revealing their flat-band potential value or the position of conduction band at 1 kHz frequency; (b) energy band positions of the BOB catalysts obtained from the UV-DRS (see Figure S1) and Mott–Schottky measurements.

is strongly required to meet the global demand for H_2O_2. The photosynthesis of H_2O_2 directly from water, via the combination of the photocatalytic two-electron reduction of O_2 and the catalytic four-electron oxidation of water, is a cleaner method.[8] The field of photocatalytic H_2O_2 production has seen several remarkable influxes over the past decade, reporting catalysts ranging from homogeneous[9,10] to heterogeneous,[11] metal[11a,d] to nonmetal variants,[1e,11c,h,12] single-component[12g,k,13] to multicomponent systems,[11a−d,12a,b,c,d,i,14] pure inorganic-[11a,d,14b,15] or organic-based materials[1e,11c,12] to their hybrids, covalent organic frameworks (COFs),[12j] metal–organic frameworks (MOFs),[16] and polymers and single-atom systems.[8,14d,17] All of these reported catalysts used either pure water or a water–alcohol mixture as the corresponding proton donor. As such, a much more attractive method for H_2O_2 generation would be a direct synthesis from seawater because the latter represents 97% of the surface water on our planet and contains 3.0–5.0% of salts along with organic and inorganic pollutants. The presence of salts leads to the deactivation of the catalysts due to lowering the light absorption, the capability of electron transfers, and lowering the bandgap and band positions, thus hampering their reactivity in seawater.[18] Although this problem has been solved by electrocatalysis and photoelectrocatalysis, the photocatalytic approach is still in its infancy.[1b,12k,19−21] Considering the high abundance of seawater, generating H_2O_2 from it should provide a sustainable solution in the H_2O_2 market. Additionally, if a green catalyst can be developed, it should meaningfully contribute to meeting the Sustainable Development Goals (SDG).[22]

Based on this background, we designed a sustainable heterogeneous photocatalyst to generate H_2O_2 from seawater.[18] Indeed, the development of catalysts from renewable resources has received high priority to reduce the utilization of fossil resources.[23,24] Biopolymers such as cellulose and lignin have garnered interest as ideal supports for heterogeneous catalysts. Lignin is an aromatic biopolymer with high carbon content (>60 atom %), high thermal stability, and biodegradability. These properties greatly enhance the designing of low-cost smart photocatalysts by changing the bandgap, eliminating the recombination of holes, and adjusting the band positions.[25,26] Combining all this information, we have chosen lignin as the biomaterial to generate H_2O_2 from seawater. In particular, BiOBr nanostructures have been hydrothermally grown under alkaline conditions on hydrolysis lignin because the latter, in opposite to other lignin types, can withstand its dissolution in such alkaline conditions.[25] This novel composite shows high stability in seawater and can be recycled several times (more than five).

RESULTS AND DISCUSSION

Recently, it has been predicted that integrated inorganic semiconductor nanostructures with lignin as substrate could result in superior photocatalytic activity for solar energy conversion.[27] This fact was the motivation behind our discovery of this type of bioinorganic photocatalysts formed by controlled hydrothermal synthesis on biobased substrates. We chose for our investigation both chitosan (CBOB) and lignin (LBOB) as substrates to grow BiOBr semiconductor nanosheets (BOB). Such bismuth oxyhalides BiOX (X = Br, Cl, I) represent a class of mixed-anion compounds that have emerged as potential photocatalysts for catalysis, energy materials, and energy conversion.[28,29] We also used graphene as the support matrix for a favorable comparison of photocatalytic activity (GBOB).

At the beginning of the characterizations, UV-DRS spectroscopy was carried out to determine the bandgap of these photocatalysts. The UV-DRS Tauc plot analyses of all these photocatalysts exhibited adequate bandgap in the visible-light region (see Figure S1) for LBOB (~2.9 eV → 427 nm), CBOB (~3.0 eV → 413 nm), and GBOB (~2.6 eV → 477 nm). In fact, an apparent modification of the bandgap has been achieved by using supports to the BOB catalysts (~3.0 eV → 413 nm). Mott–Schottky measurements revealed that the flat-band potentials or conduction band (CB) positions of the LBOB variant had the highest CB position at ca. +0.03 V vs RHE, followed by BOB at ca. +0.19 V vs RHE, CBOB at ca. +0.23 V vs RHE, and GBOB with ca. +0.59 V vs RHE (Figure 1a,b). These results suggested that all these photocatalysts are able to participate in the direct 2e$^-$ oxygen reduction reaction (**ORR**) to generate H_2O_2 as the reduction potentials of O_2 stay below +1.12 V vs RHE.[8,11f] Interestingly, only LBOB should be able to promote 2e$^-$ ORR through both the indirect and direct pathways, as shown in Scheme 2.

As the band positions of these photocatalysts were in the range for the formation of H_2O_2 from water, we added NaCl to

https://doi.org/10.1021/jacs.1c10786
J. Am. Chem. Soc. XXXX, XXX, XXX−XXX

Scheme 2. Adequate Standard Reduction Potentials for the Generation of H_2O_2[a]

Direct ORR:

$O_2 + 2\,e^- + 2\,H^+ \rightarrow H_2O_2$ ($E° = +1.12$ V vs. RHE)

Indirect ORR:

$O_2 + e^- \rightarrow O_2^{-\bullet}$ ($E° = +0.11$ V vs. RHE)

$O_2^{-\bullet} + e^- + 2\,H^+ \rightarrow H_2O_2$ ($E° = +1.88$ V vs. RHE)

[a]Note: all potential values have been converted to RHE from NHE (pH = 7.47).

pure water to mimic the average concentration (0.6 M) of the saline content in seawater. The time-dependent reaction profiles for the evaluated BOB catalysts have revealed that the LBOB variant yielded higher H_2O_2 than the remaining variants in the presence of 0.6 M NaCl (Figure 2a). Notably, while using the LBOB catalyst, the H_2O_2 concentration continued to increase even after 6 h. H_2O_2 (2100 mM) was obtained with ~8000 lx (Figure 2b). Subsequently, fresh LBOB catalyst was investigated in pure water containing a higher concentration of NaCl (0.9 M), but no yield improvement was observed.

Considering that seawater contains a plethora of dissolved metal and nonmetallic ions such as Ca^{2+}, Mg^{2+}, K^+, and SO_4^{2-} in lower amounts, we elucidated their influence on the LBOB-catalyzed H_2O_2 photoproduction. Experiments using different concentrations (0.01, 0.02, 0.03, and 0.04 M) of $CaCl_2$, $MgCl_2$, KCl, or Na_2SO_4 were conducted in pure water. A steady increase in H_2O_2 concentration with the salt concentration has been observed, and 2660 μM of H_2O_2 was formed with 0.04 M of KCl (Figure 2c).[18] Given the high H_2O_2 photoproduction in 0.6 M aq NaCl solution, we further decided to investigate the effect of other sacrificial reagents such as H_2SO_4, HCl, HCOOH, CH_3COOH, NaOH, and EtOH at 0.6 M concentration in pure water. Notably, an additional sacrificial proton donor such as acid, a hydroxy donor such as NaOH, or an electron donor such as ethanol enhanced the formation of H_2O_2 in the solution. Among all of them, HCOOH has shown the highest reactivity (Figure 2d).[13]

Having evaluated the photocatalytic performance of the LBOB catalyst in all of the major inorganic salts present in seawater, further assessments were performed in natural

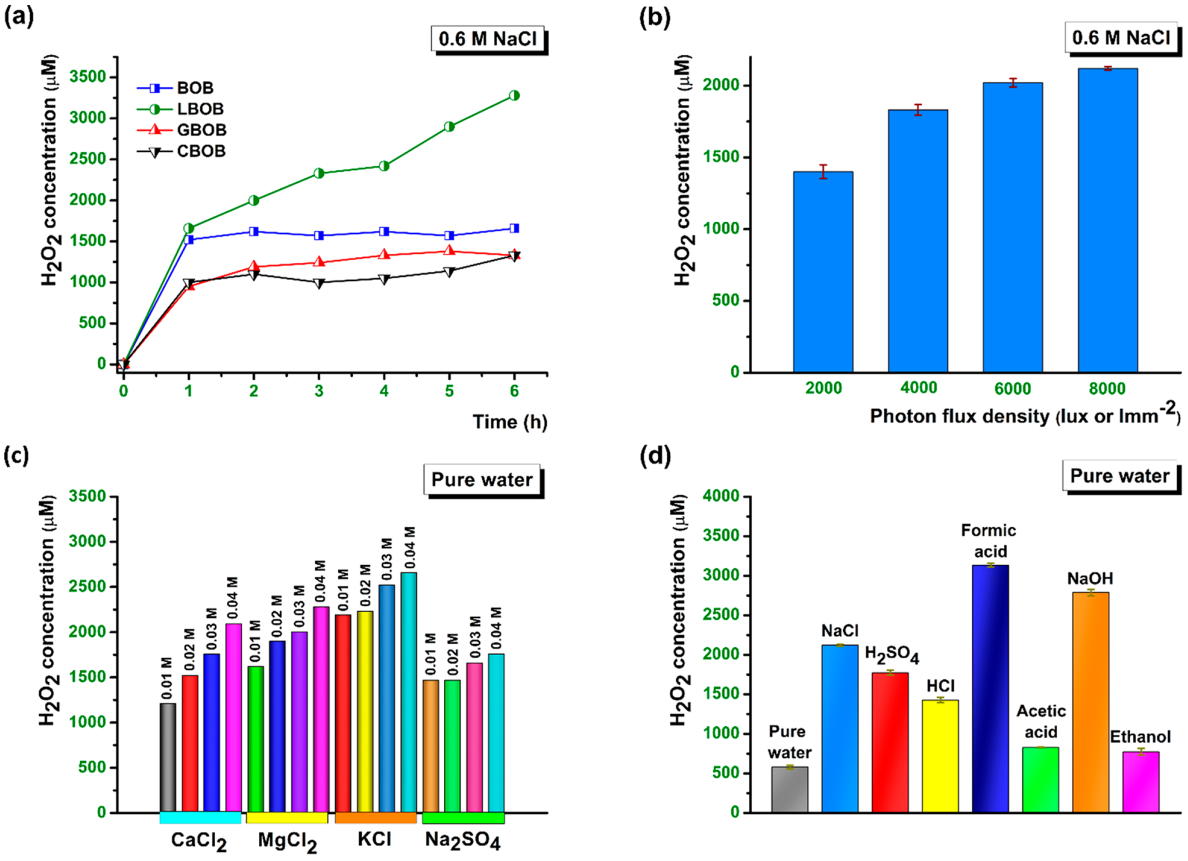

Figure 2. (a) Photocatalytic H_2O_2 production using various BOB catalysts. Used the BOB photocatalysts (1.37 g/L), pure water (33 mL), and NaCl (1.15 g). Sampling (2 mL) was done every hour. (b) Photocatalytic H_2O_2 production using the LBOB catalyst under different photon flux densities. Used 1.37 g/L LBOB catalyst, pure water (33 mL), and NaCl (1.15 g). Reaction time = 6 h. (c) Photocatalytic H_2O_2 production using the LBOB catalyst using various salts present in seawater. Used 1.37 g/L LBOB catalyst and pure water (33 mL). Reaction time = 6 h. (d) Photocatalytic H_2O_2 production using the LBOB catalyst using various acids, NaOH, and ethanol. Used 1.37 g/L LBOB catalyst and pure water (33 mL) and additives (0.6 M). Reaction time = 6 h. General reaction conditions: O_2 atmosphere (1 bar), Kessil LED lamp (λ = 427 nm). H_2O_2 concentration values were obtained using the redox titration method with aq. $KMnO_4$. All yield values in (b) and (d) are average values obtained from triplicate.

https://doi.org/10.1021/jacs.1c10786
J. Am. Chem. Soc. XXXX, XXX, XXX−XXX

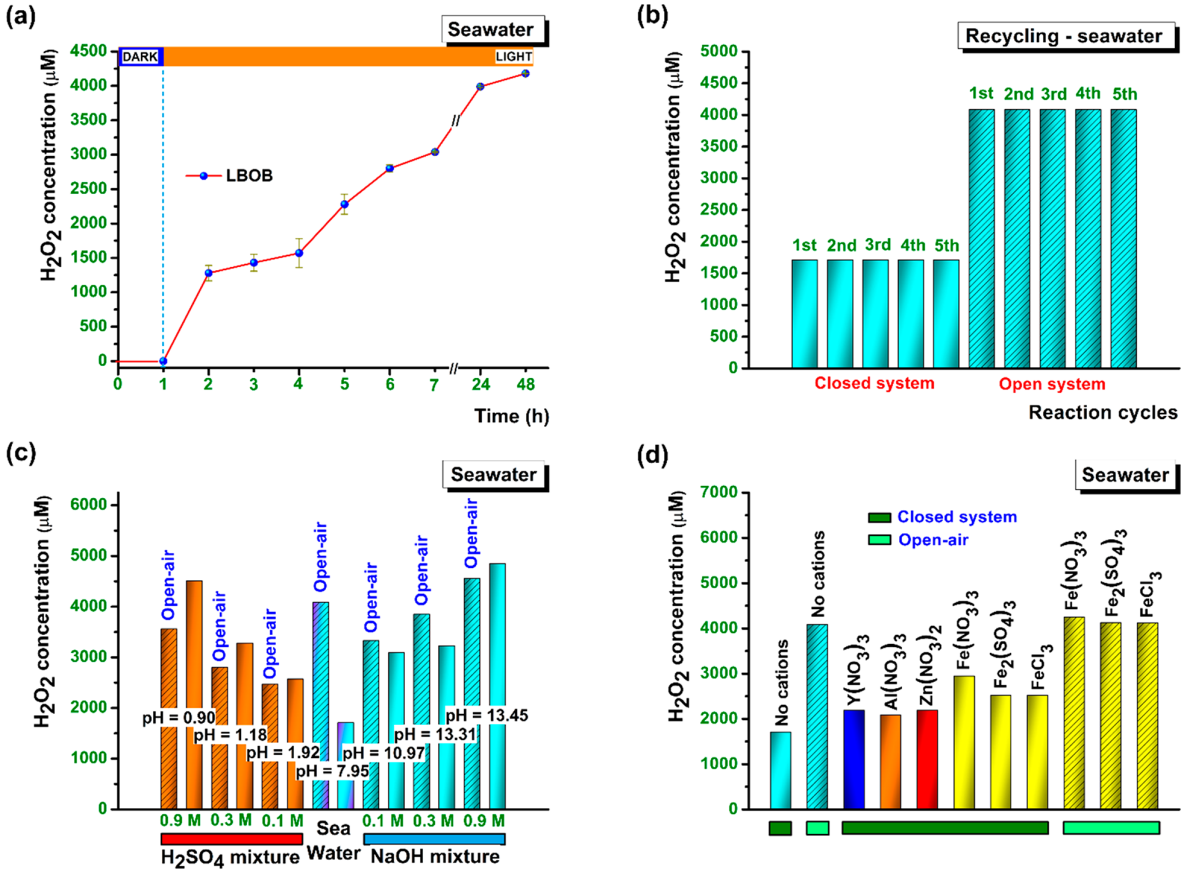

Figure 3. (a) Temporal H_2O_2 photoproduction in real seawater catalyzed by the LBOB catalyst. Sampling (2 mL) was done at each interval. (b) Recycling chart of the LBOB catalyst in closed and open-air systems. Reaction time = 6 h. (c) Photocatalytic H_2O_2 production using the LBOB catalyst in real seawater containing different concentrations of H_2SO_4 and NaOH. Reaction time = 6 h. (d) Photocatalytic H_2O_2 production using the LBOB catalyst in real seawater containing 0.04 M metal ions. Reaction time = 6 h. General reaction conditions: LBOB photocatalyst (1.37 g/L), real seawater (33 mL), O_2 atmosphere (1 bar or open-air, λ = 427 nm), stirring rate (850 rpm). H_2O_2 concentration values were obtained using the redox titration method with aq. $KMnO_4$. The yield values in (a) are averaged from the results of two reactions.

seawater. It is known that high concentrations of ions and organic components present in seawater can severely hamper photocatalytic performance by impeding their intrinsic structures and electron-transport capabilities.[18,30−32] However, as this catalyst had already shown reactivity in the presence of these salts, it was expected that this catalyst would also show reactivity in natural seawater. Indeed, the time-dependent H_2O_2 formation using the LBOB became almost linear for the first 7 h under irradiation (Figure 3a), and the H_2O_2 concentration was highly stable even after 48 h of irradiation. In a standalone reaction (in O_2 atmosphere, closed system) in natural seawater, a respectable H_2O_2 concentration of 1710 μM was obtained after 6 h, which is ca. 3 times higher than in pure water (580 μM). We could speculate that this result is probably due to the presence of organic functional groups (primarily, the phenol moiety) in the lignin support that gets ionized and acts as an electron sink in the presence of metal ions[18] or aqueous NaCl, $CaCl_2$, $MgCl_2$, KCl, and Na_2SO_4 solutions serving as a weak Bronsted−Lowry base that can extract the proton from the phenol moiety. Notably, the H_2O_2 concentration in the time-dependent reaction is higher than a standalone reaction of 6 h using the same reaction flask as water volume decreases with sampling albeit being illuminated under the same light intensity. Higher light penetration is achieved after each sampling enabling intensified photoreaction.

The LBOB catalyst was then investigated for recyclability in natural seawater in a closed (in O_2 atmosphere) system. As shown in Figure 3b, the H_2O_2 concentration remained at 1710 μM for five reaction cycles, indicating that the LBOB catalyst is highly stable in seawater. The photocatalytic H_2O_2 production in natural seawater using the LBOB catalyst was also evaluated in open air. A higher amount of H_2O_2 (4085 μM) was obtained in 6 h, which was more than twice the amount of H_2O_2 produced in a closed system (1710 μM) (see Figures 3b,c). This unprecedented result is due to the efficient adsorption−desorption of O_2 molecules on the surface of the LBOB catalyst. The reactive oxygen species (ROS) was further determined to be $O_2^{\bullet-}$ through spin-trapped EPR experiments using DMPO (see Figures S2 and S3, Table S1). Upon illumination, a clear EPR signal for the DMPO-OOH spin-trapped adduct could be observed in the EPR spectra.

Considering the high H_2O_2 photoproduction in natural seawater, we decided to investigate the effect of a conventional acid, H_2SO_4, and a base, NaOH. For this reason, we studied these additives at different concentrations (0.1, 0.3, and 0.9 M), as shown in Figure 3c. H_2O_2 photoproduction was seen to increase several times compared to the results obtained with

https://doi.org/10.1021/jacs.1c10786
J. Am. Chem. Soc. XXXX, XXX, XXX−XXX

0.6 M H_2SO_4 and NaOH in pure water shown before (Figure 2d). Furthermore, slightly higher H_2O_2 concentrations were obtained with higher pH due to the deprotonating effect of NaOH with the −OH group in the lignin component of the LBOB catalyst, thereby making the lignin an electron sink similar to a previous report.[18] Notably, the collected seawater itself was slightly basic, with a measured pH value of 7.95.

Furthermore, the possibility of a cation-enhancement effect in H_2O_2 photoproduction was also investigated using various metal nitrates similar to a previous report.[10] Natural seawater containing 0.04 M Y^{3+}, Al^{3+}, Zn^{2+}, and Fe^{3+} nitrates was investigated with the LBOB catalyst. The highest H_2O_2 concentration was obtained with $Fe(NO_3)_3{\cdot}9H_2O$ (2950 μM) followed by Y^{3+} and Zn^{2+} to yield 2190 μM each and Al^{3+} yielding 2090 μM (Figure 3d). Since there was a higher H_2O_2 yield in all cases with trivalent and divalent metal ions when compared to seawater, it is safe to assume that Fenton-type reactions that can rapidly decompose H_2O_2 were suppressed or nonexistent. These values were indeed higher than the case with no extra metal ions (1710 μM). This result was due to the possible metal cation (M^{n+}) reduction by the $O_2^{\bullet-}$ radical [obtained by the action of LBOB photocatalyst (subeq 1 in Scheme 3)] (see subeq 2 in Scheme 3), followed by its oxidation (subeq 3 in Scheme 3), thereby generating H_2O_2. Another oxidation step with the O_2 molecule can regenerate the $O_2^{\bullet-}$ radical (subeq 4 in Scheme 3).

Scheme 3. Possible Explanation for the Enhancement of H_2O_2 Production in the Presence of Metal Ions and Organic Ligands (From Seawater or Lignin Support)

$$O_2 + e^- \rightarrow O_2^{-\bullet} \qquad (E^\circ = +0.14\ \text{V vs. RHE, pH} = 7.95) \qquad (1)$$

$$O_2^{-\bullet} + M^{n+}L \rightarrow M^{(n-1)+}L + O_2 \qquad (2)$$

$$O_2^{-\bullet} + M^{(n-1)+}L + 2\,H^+ \rightarrow M^{n+}L + H_2O_2 \qquad (3)$$

$$O_2 + M^{(n-1)+}L \rightarrow M^{n+}L + O_2^{-\bullet} \qquad (4)$$

It should be noted that seawater typically contains various organic molecules that can form complexes with metal ions. A previous study with coastal seawater has elucidated the role of dissolved Fe^{3+}-based organic complexes to produce H_2O_2 and the possible redox chemistry involved with O_2 and $O_2^{\bullet-}$.[33] Considering the higher performance of $Fe(NO_3)_3{\cdot}9H_2O$ for the LBOB-catalyzed H_2O_2 photoproduction, we decided to explore other inorganic salts with Fe^{3+} ions such as $FeCl_3$ and $Fe_2(SO_4)_3{\cdot}xH_2O$ as well. Delightfully, both $FeCl_3$ and $Fe_2(SO_4)_3{\cdot}xH_2O$ yielded 2520 μM H_2O_2 (Figure 3c). Nevertheless, the open-air reactions using the Fe^{3+} salts in seawater with the LBOB catalyst yielded a high H_2O_2 content of about 4000 μM.

After having investigated all the catalytic experiments, we characterized the lignin support in the LBOB material. It should be noted that the structural characterization of lignin-based materials is challenging both from a theoretical and experimental point of view due to the complexity/variety of the structures and insufficient resolution of optical spectroscopy techniques like IR, Raman, or UV−vis. Moreover, limited information is discernible from wet chemistry analysis. Hence, we flanked the experiments with classical reactive molecular dynamics simulations (ReaxFF flavor) in complex environments containing water molecules, Na^+ ions (as in seawater), a BiOBr substrate made of several layers and oxygen molecules, and quantum chemistry calculations to characterize in detail the reaction mechanisms at the interfaces. Experimentally, we used solid-state nuclear magnetic resonance (NMR) spectroscopy.[25,34] The solid-state ^{1}H MAS (Magic-angle spinning) and ^{1}H−^{13}C CPMAS (cross-polarization MAS) NMR spectra of the LBOB catalyst and hydrolysis lignin's chemical structure are shown in Figure 4a−c, respectively. The proton spectrum reveals resonances at 6.6, 3.6, and 1.3 ppm, which are attributed to aromatic, methoxy (−OCH_3), and aliphatic protons, respectively. The signals of aromatic protons and −OCH_3 groups are dominant, which indicates that a small amount of aliphatic fragments is present in the material. In the ^{1}H−^{13}C CPMAS spectrum (Figure 4b), the ^{13}C NMR signals in the chemical shift range of 100−125 ppm correspond to the aromatic C−H carbon atoms and 125−135 ppm to the C−C linkages. The signals in the range of 70−90 ppm correspond to C-α, C-β, and C-γ carbon atoms with −OH groups and those involved in − O−alkyl ether moieties. Resonances in the 50−65 ppm range can be attributed to −OCH_3 groups. The signal intensities in the chemical shift range ∼30 ppm and below are small, which indicates a low amount of −CH_3 groups and other saturated aliphatic fragments in agreement with the proton spectrum. Based on the post-mortem ^{1}H NMR analysis after photocatalysis in seawater, no changes either in relative signal intensities or peak positions were observed for the dominant resonances of aromatic and methoxy protons. This indicates that the chemical structure of the majority of the lignin component is preserved (Figure S4). Details regarding the quantification of H_2O_2 via quantitative ^{1}H NMR based on derivatization of organic molecules and its drawbacks in this work are elucidated in section S2.4.

The analysis of the reactive molecular dynamics simulations data (see section S3) suggests that, depending on the position and orientations of the lignin molecules relative to the support, some of their chains were prone to react, releasing hydrogens to the nearby support and water molecules in solution (see Figures 4d−f). This result is apparent in Figure 4e,f, which highlights the presence of isolated hydrogens below the lignin model (that become part of the BiOBr top layer) and reveal the appearance of a few water molecules produced by the reactions of lignin with the surrounding environment, close to the biomolecule. We could observe frequent exchanges of hydrogens among lignin, the substrate, and water molecules, suggesting a significant reactivity at the oxide/organic interface and a remarkable accumulation of sodium ions and oxygen molecules there.

Moving to the experimental characterization of the lignin-based support (in the material) and the catalyst stability during the reaction, we confirmed that the PXRD patterns of the sample before and after the reaction (see Figure 5a) could be indexed as BiOBr[35] using the crystallographic data from JCPDS-01-085-0862, which proved that the photocatalyst was a single-phase BiOBr. The surface composition of the pristine catalyst was also investigated by XPS. The corresponding XPS Bi 4f spectrum showed two main components, $4f_{7/2}$ and $4f_{5/2}$, due to the spin−orbit splitting (Figure 5b,c). The asymmetric shape of these peaks indicated the presence of various forms of Bi on the surface. Bi^{3+} species in the BiOBr (doublet at 159.6 eV ($4f_{7/2}$) and 164.9 eV ($4f_{5/2}$)) and Bi_2O_3 (158.8 and 164.1 eV, respectively) phases were definitely dominant.[36,37] Nevertheless, Bi^{5+} species appeared additionally in the sample. The doublet confirmed their presence at 160.7 eV ($4f_{7/2}$) and 165.9 eV ($4f_{5/2}$).[38] Notably, Bi^{5+} constitutes only approximately 5% of all Bi atoms accumulated on the surface (see Figure 5b). In

https://doi.org/10.1021/jacs.1c10786
J. Am. Chem. Soc. XXXX, XXX, XXX−XXX

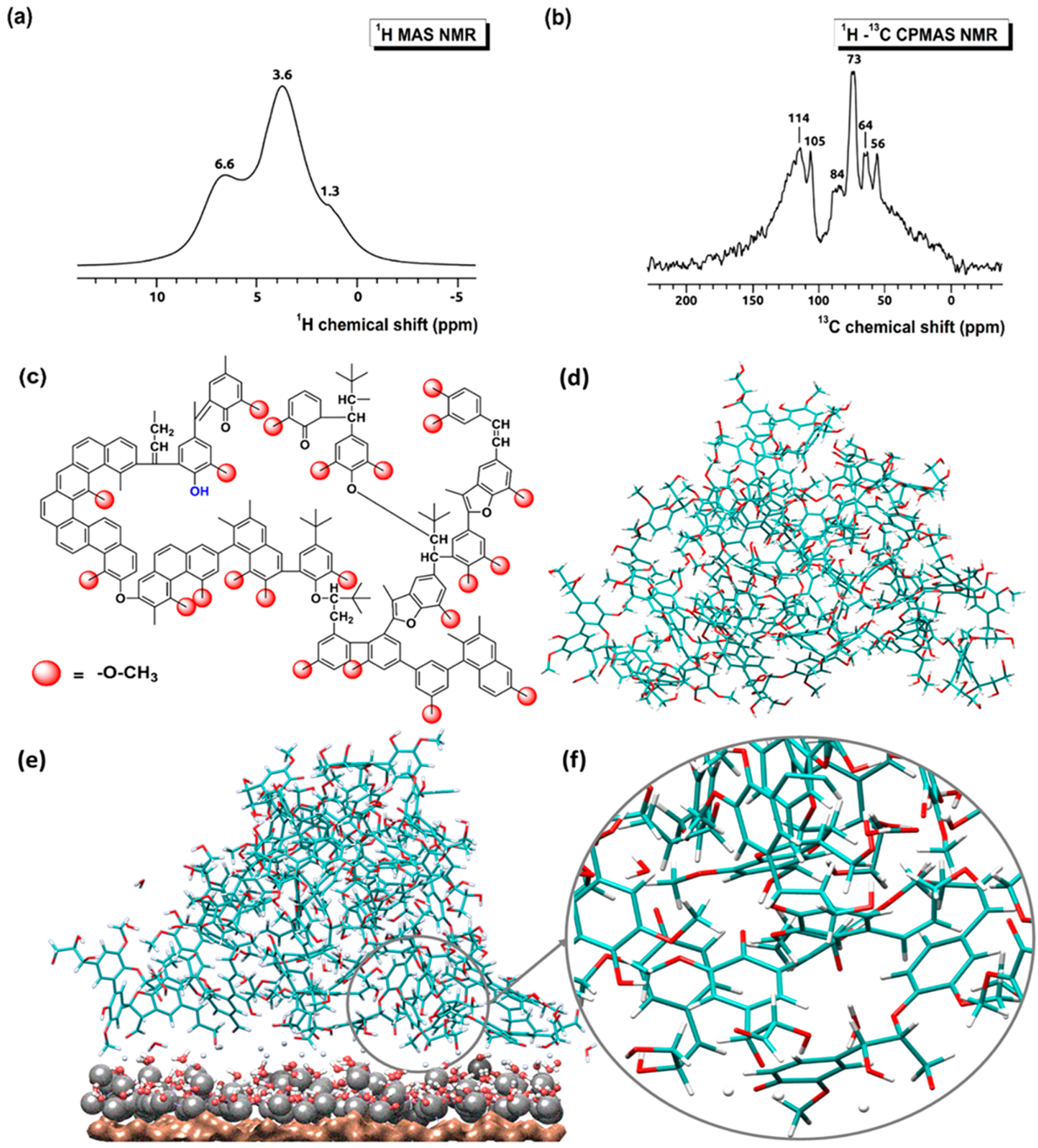

Figure 4. (a) ^{1}H MAS NMR, (b) ^{1}H−^{13}C CPMAS spectra of the LBOB catalyst collected at 14.1 T and 60 kHz MAS, and (c) structure of hydrolysis lignin, (d) molecular model in water solution, (e) lignin model in a reactive water environment in contact with a BiOBr model (downshifted relative to its original position to highlight the exchange of hydrogens), (f) magnified view of a portion of the molecule at the interface (the surrounding bulk water molecules and ions are not displayed for clarity). Color codes: Bi, gray; Br, brown; C, cyan; O, red; H, white.

the sample after the reaction, this component was not observed, indicating a partial surface reduction. The XPS O 1s spectra (see Figure 5c), with two essential peaks at 530.2 ± 0.1 eV (attributed to O^{2-} in the inorganic part of the composite) and 532.5 eV (mainly −OH in lignin), confirmed such an explanation.[39] The sample after the reaction exhibited an apparent decrease in the intensity of the peak corresponding to the O^{2-} species.

The O/Bi atomic ratio on the surface decreased during the process from 1.57 to 1.45. The TEM and HR-TEM images of the samples before and after the reaction are shown in parts d and e, respectively, of Figure 5. The lattice spacing from HRTEM images and SAED patterns of both samples showed the BiOBr phase (JCPDS-01-085-0862), which is in agreement with the PXRD analysis. However, the grain size of the sample after the reaction tends to be larger than that of the sample before the reaction. The HAADF-STEM EDX elemental maps shown in Figure 5f ,g show localized and no apparent differences in the elemental compositions before and after the

https://doi.org/10.1021/jacs.1c10786
J. Am. Chem. Soc. XXXX, XXX, XXX−XXX

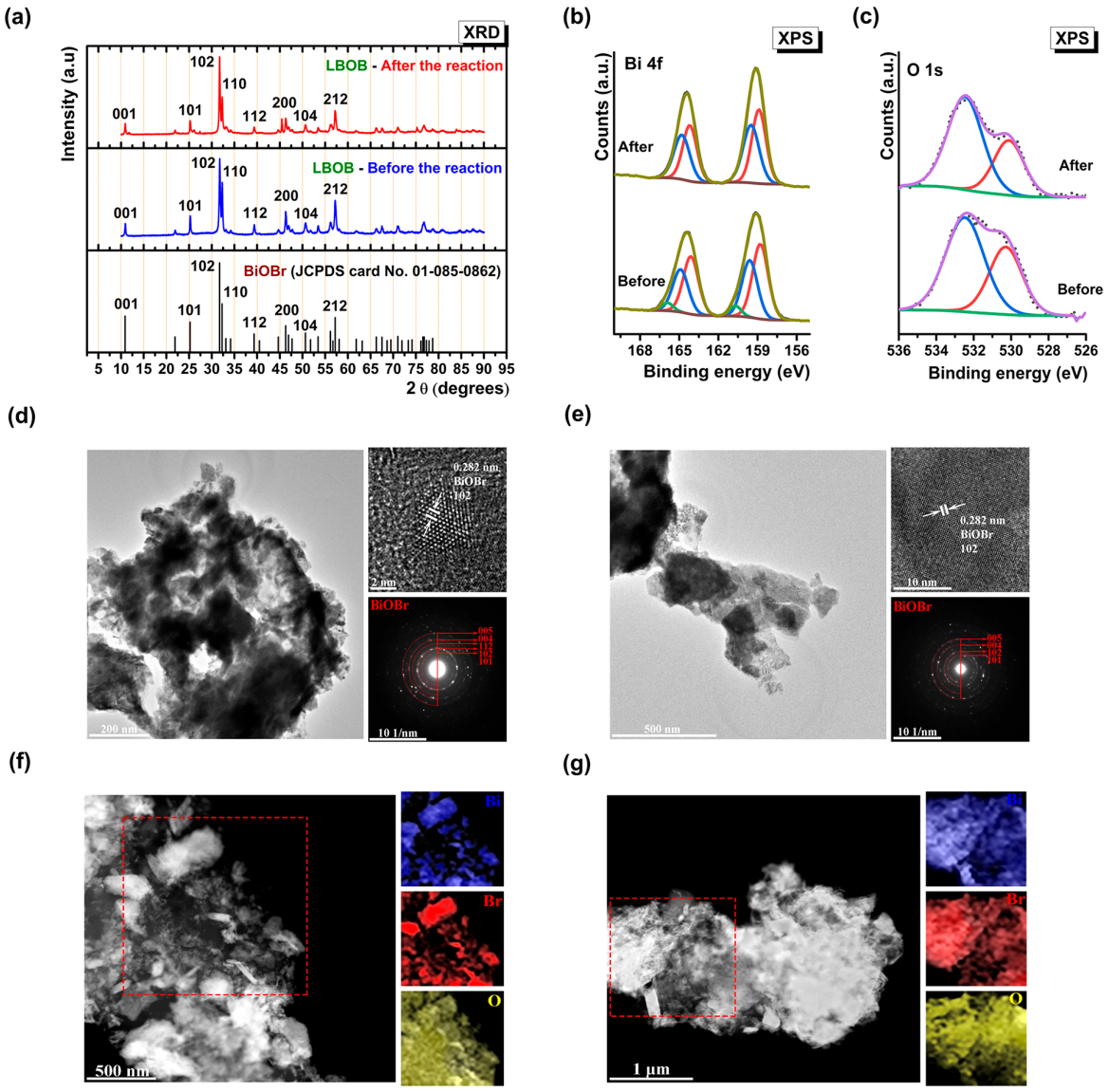

Figure 5. (a) Powder XRD patterns of the LBOB catalyst before and after the reaction in real seawater, confirming the structural stability in these conditions. (b) XPS Bi 4f spectra of the LBOB catalyst showing the chemical nature of superficial bismuth before and after the reaction in real seawater. (c) XPS O 1s spectra of the LBOB catalyst showing the chemical nature of superficial oxygen before and after the reaction in real seawater. (d) TEM, HR-TEM, and SAED images of the LBOB catalyst before the reaction in real seawater. (e) TEM, HR-TEM, and SAED images of the LBOB catalyst after the reaction in real seawater. (f) HAADF-STEM-EDX elemental maps of the fresh LBOB catalyst. (g) HAADF-STEM-EDX elemental maps of the LBOB catalyst after the reaction. Reaction conditions: LBOB photocatalyst (1.37 g/L), real seawater (33 mL), O_2 atmosphere (1 bar), Kessil LED lamp (λ = 427 nm), time (6 h), and stirring rate (850 rpm). Complementary HAADF-STEM EDX elemental mapping of the photocatalyst after reaction in NaOH or NaCl confirms the overlap of bismuth, oxygen, and bromine signals on the nanosheets (see Figures S13 and S14). For photocatalysis in 0.9 M NaOH in seawater for a longer period of time, powder XRD patterns indicate a transition toward a mixed phase BiOBr/$Bi_4O_5Br_2$, whereas photocatalysis in 0.6 M NaCl in pure water confirms structural stability of the phase BiOBr (see Figure S15).

photocatalytic reactions in seawater. These results indicated the high reusability of the LBOB catalyst.

Once we had characterized the material, we moved to the mechanistic investigations of the reaction. We used isotopically enriched $^{18}O_2$ instead of normal $^{16}O_2$ to determine the source of O_2 for the H_2O_2 formation (see section S2.5). From the GC−MS spectrum (Figure S8), it was evident that the source of oxygen in H_2O_2 was indeed O_2 gas. On the other hand, the superoxide radical anion (presence confirmed via EPR, see section S2.2 for more details) was the key reactive oxygen species in this reaction which was generated by the electron transfer from the CB of the LBOB catalyst.

Comparative MS plot of pure graphene is shown in Figure S9. To decipher the nature of the charge-transfer between the BOB catalysts and the O_2 gas, electrochemical impedance spectroscopy (EIS) measurements were performed. As shown in Figure 6, the LBOB catalyst showed minimum curve size in O_2 saturated condition under illumination (λ = 427 nm) compared to other BOB catalysts and the bare FTO electrode, indicating efficient charge transfer. This result was further

https://doi.org/10.1021/jacs.1c10786
J. Am. Chem. Soc. XXXX, XXX, XXX−XXX

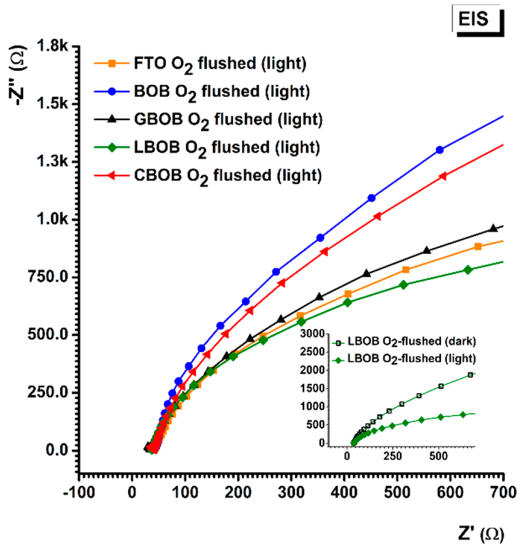

Figure 6. EIS Nyquist spectra of the BOB catalysts under irradiated conditions (Kessil LED lamp, λ = 427 nm) in the presence of O_2 saturated electrolyte [150 mL, aq NaCl (150 mM), $K_4Fe(CN)_6$ (1 mM), and $K_3Fe(CN)_6$ (1 mM)]. The EIS plot of the bare FTO working electrode is also shown. EIS Nyquist plot of the LBOB catalyst in O_2 saturated condition with and without irradiation is shown in the inset. Notably, the EIS of the LBOB is smaller than all other BOB catalysts denoting a higher charge transfer in the presence of O_2 under irradiation.

supplemented by the cyclic voltammetry studies conducted using rotating disc electrode (RDE) attachment with a glassy carbon electrode (GC) (Figures S10 and S11). It was clear that the LBOB catalyst predominantly exhibited indirect ORR in O_2 saturated conditions (see Scheme 2). Additionally, the linear sweep voltammetry measurements conducted directly in seawater show a considerable increase in photocurrent for the oxygen evolution reaction (OER) at an onset potential of ca. +1.7 V vs RHE in the presence of light (Figure S12a,b), which is also a parallel photocatalytic reaction occurring with ORR. This result is indicative of an efficient seawater oxidation photocatalyst. Also, the onset potential value for the ORR was seen at ca. +0.6 V vs RHE (Figure S12c,d), indicating the catalytic reduction of O_2. Notably, the peak photocurrent difference in the dark and illuminated conditions is apparently closer than with water oxidation, denoting a high oxygen reduction capability of the LBOB catalyst.

According to the literature, when an ionic salt was introduced into pure water, the lignin support could act as the electron sink, enhancing the hole−electron separation, justifying the improvement of the photocatalytic efficiency.[18] In the presence of a base −NaOH, the reaction mechanism initially proceeded as in the case of highly electropositive ions but also acted as a source of $^{\bullet}OH$ radical (which dimerizes to form H_2O_2) formed by the hole-mediated oxidation of ^{-}OH ions and therefore yielded a high amount of H_2O_2. This reason is also relevant to the results obtained with seawater in different pH, where a higher pH yielded high H_2O_2 concentrations.

An atomic level understanding of all these processes could be obtained by extracting, from the production trajectories, a few representative portions of the sampled configurations and carrying out quantum chemistry calculations focused on the O_2 transformation reactions at the oxide/lignin interface. The atomistic scenario suggested that the neutral O_2 molecule could be adsorbed near the surface before irradiation, in the arrangement shown in Figure 7a, adopting a gas-phase triplet

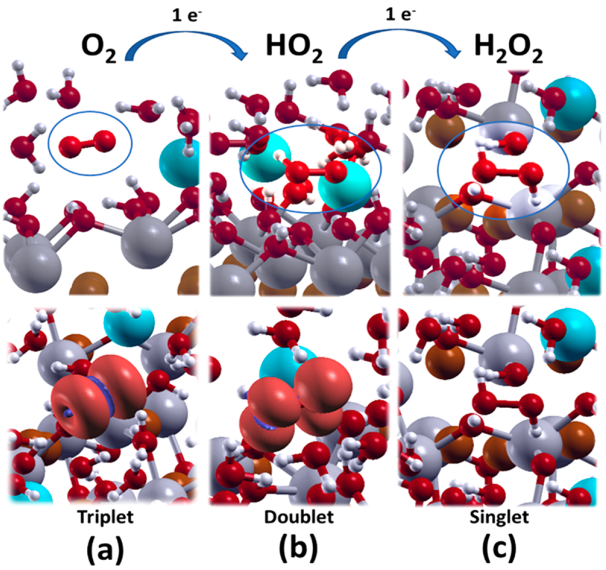

Figure 7. (Top) Atomistic evolution of molecular oxygen into hydrogen peroxide via addition of two electrons at the BiOBr interface in the presence of water and Na^+ ions (cyan spheres). (Bottom) Spin density evolving from triplet state (neutral oxygen molecule) to doublet (neutral HO_2 intermediate) to singlet (neutral H_2O_2 final product). Bi gray, Br brown, O red, H white, Na^+ (cyan).

spin configuration. When one electron is injected into the system (by mimicking the action of the UV irradiation), the molecular oxygen becomes negatively charged and approaches the surface by strongly interacting with both terminal −OH groups of BiOBr and the neighboring water molecules through a dense network of hydrogen bonds (see section S3). Then its spin state is lowered to a doublet with a consequent breaking of the cylindrical symmetry of the spin density with respect to the initial state. The density of states (DOS) (Figure S17b) shows that the molecular oxygen 2p states are shifted to higher energies and fall within the oxide bandgap. In this "excited" configuration, the HO_2 complex shown in Figure 7b is spontaneously formed via the extraction of selected hydroxyl groups from the oxide surface.

On the contrary, a similar process does not occur for the neutral oxygen molecules (the HO_2 complex was hardly stabilized), which is in agreement with the experimental observation that the catalyst must be activated by UV irradiation. The HO_2 complex is also characterized by the same doublet state of the negatively charged oxygen molecule before the proton transfer. Injection of a further electron in the system allows for the formation of H_2O_2, as the HO_2 complex evolves toward the final product by extracting a second proton from the oxide surface, thus quenching the total spin state of the system to a singlet configuration (Figure 7c). According to the results of the RMD, the depletion of protons from the oxide surface, which accompanies the oxygen reduction, can be compensated by the process of back-donation of protons and hydrogen atoms extracted from lignin.

https://doi.org/10.1021/jacs.1c10786
J. Am. Chem. Soc. XXXX, XXX, XXX−XXX

As shown in Figure 7, all the configurations see the adsorption of sodium ions above the oxide surface in the neighborhood of the oxygen molecules. To disclose the role played by these ions in the oxygen reduction process, we have simulated the first step of the reaction by moving the ions away from the oxide surface. The final results indicate that the HO_2 complex is stable but higher in energy by about 24 kcal/mol than the initial state, corresponding to the negatively charged oxygen molecule before the first proton transfer. This quantity (although not large) should be compared with the negligible cost which accompanies the proton transfer when the sodium ions are adsorbed near the oxide surface, suggesting that positive ions could stabilize the negative charge accumulated on the oxide surface after the proton transfer to the oxygen molecule. All the details of the modeling activity are reported in the Supporting Information.

Considering all the presented experimental and theoretical results, we suggest that, upon being irradiated under visible light (λ = 427 nm), the LBOB catalyst easily absorbed the photon energy to generate electron−hole pairs to facilitate multiple parallel reactions on its surface.

CONCLUSIONS

We have demonstrated that biomass (hydrolysis lignin) supported BiOBr is a robust photocatalyst for the production of H_2O_2 from natural seawater under visible light (λ = 427 nm). The photocatalytic performance of the lignin-supported BiOBr catalyst was pitched against other supported BiOBr variants, e.g., chitosan and graphene, as well as the unsupported variant. The enhanced performance of the LBOB catalyst stems mainly from the addition of the lignin biopolymer, which lowers the reduction potential of the catalyst without sacrificing the visible light absorption capability. Moreover, the organic functional groups present in the lignin support acts as an electron sink on ionization with the metal ions present in the seawater (through Bronsted−Lowry base proton abstraction), thereby giving the LBOB catalyst a significant edge in performance with seawater over pure water (1710 vs 580 μM). The photocatalytic performance of the LBOB catalyst was investigated with acidic and basic seawater mixtures, where a higher performance was obtained with highly basic systems. The presence of divalent and trivalent transition metal ions in seawater enhanced the H_2O_2 photoproduction with the help of the LBOB catalyst, with Fe^{3+} ions yielding the highest H_2O_2 concentration.

Open-air reactions consistently yielded over 2.3 times H_2O_2 photoproduction from natural seawater, a promising and practical way of obtaining H_2O_2 economically and efficiently. Additionally, the LBOB catalyst was active for at least 48 h and was recycled at least five times without losing any catalytic activity. The critical advancement of this report is the demonstration of lignin as a magnifier of the photocatalytic activity for H_2O_2 production from seawater. The reaction mechanism was deciphered through experimental results supplemented with detailed physicochemical characterization techniques and multiscale/level modeling. We believe that related lignin-photocatalyst systems could also be potentially powerful catalysts for photoredox-driven organic reactions.

ASSOCIATED CONTENT

Supporting Information

The Supporting Information is available free of charge at https://pubs.acs.org/doi/10.1021/jacs.1c10786.

All experimental procedures, extended characterization details and computational characterization details are available in the document (PDF)

AUTHOR INFORMATION

Corresponding Authors

Shoubhik Das − *Department of Chemistry, Universiteit Antwerpen, Antwerp 2020, Belgium;* orcid.org/0000-0002-4577-438X; Email: shoubhik.das@uantwerpen.be

Adam Slabon − *Department of Materials and Environmental Chemistry, Stockholm University, Stockholm 10691, Sweden;* orcid.org/0000-0002-4452-1831; Email: adam.slabon@mmk.su.se

Authors

Aswin Gopakumar − *Department of Chemistry, Universiteit Antwerpen, Antwerp 2020, Belgium*

Peng Ren − *Department of Chemistry, Universiteit Antwerpen, Antwerp 2020, Belgium*

Jianhong Chen − *Department of Materials and Environmental Chemistry, Stockholm University, Stockholm 10691, Sweden*

Bruno Vinicius Manzolli Rodrigues − *Department of Materials and Environmental Chemistry, Stockholm University, Stockholm 10691, Sweden*

H. Y. Vincent Ching − *Department of Chemistry, Universiteitsplein 1, Universiteit Antwerpen, Wilrijk 2610, Belgium*

Aleksander Jaworski − *Department of Materials and Environmental Chemistry, Stockholm University, Stockholm 10691, Sweden;* orcid.org/0000-0002-7156-559X

Sabine Van Doorslaer − *Department of Chemistry, Universiteitsplein 1, Universiteit Antwerpen, Wilrijk 2610, Belgium;* orcid.org/0000-0002-1685-9202

Anna Rokicińska − *Faculty of Chemistry, Gronostajowa 2, Jagiellonian University, Kraków 30-387, Poland;* orcid.org/0000-0001-8397-4422

Piotr Kuśtrowski − *Faculty of Chemistry, Gronostajowa 2, Jagiellonian University, Kraków 30-387, Poland;* orcid.org/0000-0001-8496-0559

Giovanni Barcaro − *CNR-IPCF, Institute for Chemical and Physical Processes, Area della Ricerca, Pisa I-56124, Italy;* orcid.org/0000-0002-5520-5914

Susanna Monti − *CNR-ICCOM, Institute of Chemistry of Organometallic Compounds, Area della Ricerca, Pisa I-56124, Italy;* orcid.org/0000-0002-3419-7118

Complete contact information is available at: https://pubs.acs.org/10.1021/jacs.1c10786

Author Contributions

The manuscript was written through contributions of all authors. All authors have given approval to the final version of the manuscript.

Notes

The authors declare no competing financial interest.

ACKNOWLEDGMENTS

We acknowledge financial support from an IOF grant from UAntwerpen, Belgium. A.S. thanks the Swedish Energy Agency for financial support (project no: 50501-1). We also thank Mr. Tong Zhang, Mr. Jian Zhu, and Mr. Shahid Ullah Khan, UAntwerpen, Belgium, for helpful discussions. S.M. thanks

Loukas Petridis and Jeremy C. Smith for providing her with the lignin coordinates extracted from their simulations. S.M. is grateful to Adri C. T. van Duin for the reactive force field parameters describing BiO systems and valuable suggestions.

REFERENCES

(1) (a) Perry, S. C.; Pangotra, D.; Vieira, L.; Csepei, L.-I.; Sieber, V.; Wang, L.; Ponce de León, C.; Walsh, F. C. Electrochemical synthesis of hydrogen peroxide from water and oxygen. *Nat. Rev. Chem.* **2019**, *3*, 442−458. (b) Xue, Y.; Wang, Y.; Pan, Z.; Sayama, K. Electrochemical and Photoelectrochemical Water Oxidation for Hydrogen Peroxide Production. *Angew. Chem., Int. Ed.* **2021**, *60*, 10469−10480; *Angew. Chem.* **2021**, *133*, 10561−10572. (c) Kim, J.; Chung, Y.-M.; Kang, S.-M.; Choi, C.-H.; Kim, B.-Y.; Kwon, Y.-T.; Kim, T. J.; Oh, S.-H.; Lee, C.-S. Palladium nanocatalysts immobilized on functionalized resin for the direct synthesis of hydrogen peroxide from hydrogen and oxygen. *ACS Catal.* **2012**, *2*, 1042−1048. (d) García-Serna, J.; Moreno, T.; Biasi, P.; Cocero, M. J.; Mikkola, J.-P.; Salmi, T. O. Engineering in direct synthesis of hydrogen peroxide: targets, reactors and guidelines for operational conditions. *Green Chem.* **2014**, *16*, 2320−2343. (e) Zeng, X.; Liu, Y.; Kang, Y.; Li, Q.; Xia, Y.; Zhu, Y.; Hou, H.; Uddin, M. H.; Gengenbach, T. R.; Xia, D.; Sun, C.; Mccarthy, D. T.; Deletic, A.; Yu, J.; Zhang, X. Simultaneously Tuning Charge Separation and Oxygen Reduction Pathway on Graphitic Carbon Nitride by Polyethylenimine for Boosted Photocatalytic Hydrogen Peroxide Production. *ACS Catal.* **2020**, *10*, 3697−3706. (f) Liu, J.; Zou, Y.; Jin, B.; Zhang, K.; Park, J. H. Hydrogen Peroxide Production from Solar Water Oxidation. *ACS Energy Lett.* **2019**, *4*, 3018−3027.

(2) (a) Staffell, I.; Scamman, D.; Abad, A. V.; Balcombe, P.; Dodds, P. E.; Ekins, P.; Shah, N.; Ward, K. R. The role of hydrogen and fuel cells in the global energy system. *Energy Environ. Sci.* **2019**, *12*, 463−491. (b) Hart, D.; Howes, J.; Lehner, F.; Dodds, P.; Hughes, N.; Fais, B.; Sabio, N.; Crowther, M. Scenarios for deployment of hydrogen in contributing to meeting carbon budgets and the 2050 target, UCL, London, 2015. (c) Andersson, J.; Gronkvist, S. Large-scale storage of hydrogen. *Int. J. Hydrog. Energy* **2019**, *44*, 11901−11919.

(3) Disselkamp, R. S. Can aqueous hydrogen peroxide be used as a stand-alone energy source? *Int. J. of Hydrog. Energy* **2010**, *35*, 1049−1053.

(4) McDonnell-Worth, C. J.; MacFarlane, D. R. Progress Towards Direct Hydrogen Peroxide Fuel Cells (DHPFCs) as an Energy Storage Concept. *Aust. J. Chem.* **2018**, *71*, 781−788.

(5) Expert Market Research. Global Hydrogen Peroxide Market Report and Forecast 2021−2026, https://www.expertmarketresearch.com/reports/hydrogen-peroxide-market (accessed 2021-09-01).

(6) Myers, R. *The 100 Most Important Chemical Compounds*; Greenwood Publishing Group: Westport, CT, 2007.

(7) Campos-Martin, J. M.; Blanco-Brieva, G.; Fierro, J. L. G. Hydrogen Peroxide Synthesis: An Outlook beyond the Anthraquinone Process. *Angew. Chem., Int. Ed.* **2006**, *45*, 6962−6984.

(8) Zeng, X.; Liu, Y.; Hu, X.; Zhang, X. Photoredox catalysis over semiconductors for light-driven hydrogen peroxide production. *Green Chem.* **2021**, *23*, 1466−1494.

(9) Węcławski, M. K.; Jakešová, M.; Charyton, M.; Demitri, N.; Koszarna, B.; Oppelt, K.; Sariciftci, S.; Gryko, D. T.; Daniel Głowacki, E. Biscoumarin-containing acenes as stable organic semiconductors for photocatalytic oxygen reduction to hydrogen peroxide. *J. Mater. Chem. A* **2017**, *5*, 20780−20788.

(10) Kato, S.; Jung, J.; Suenobu, T.; Fukuzumi, S. Production of hydrogen peroxide as a sustainable solar fuel from water and dioxygen. *Energy Environ. Sci.* **2013**, *6*, 3756−3764.

(11) (a) Chu, C.; Huang, D.; Zhu, Q.; Stavitski, E.; Spies, J. A.; Pan, Z.; Mao, J.; Xin, H. L.; Schmuttenmaer, C. A.; Hu, S.; Kim, J.-H. Electronic Tuning of Metal Nanoparticles for Highly Efficient Photocatalytic Hydrogen Peroxide Production. *ACS Catal.* **2019**, *9*, 626−631. (b) Moon, G.; Kim, W.; Bokare, A. D.; Sung, N.; Choi, W. Solar production of H_2O_2 on reduced graphene oxide−TiO_2 hybrid photocatalysts consisting of earth-abundant elements only. *Energy Environ. Sci.* **2014**, *7*, 4023−4028. (c) Shiraishi, Y.; Takii, T.; Hagi, T.; Mori, S.; Kofuji, Y.; Kitagawa, Y.; Tanaka, S.; Ichikawa, S.; Hirai, T. Resorcinol−formaldehyde resins as metal-free semiconductor photocatalysts for solar-to-hydrogen peroxide energy conversion. *Nat. Mater.* **2019**, *18*, 985−993. (d) Hirakawa, H.; Shiota, S.; Shiraishi, Y.; Sakamoto, H.; Ichikawa, S.; Hirai, T. Au Nanoparticles Supported on $BiVO_4$: Effective Inorganic Photocatalysts for H_2O_2 Production from Water and O_2 under Visible Light. *ACS Catal.* **2016**, *6*, 4976−4982. (e) Liu, J.; Liu, Y.; Liu, N.; Han, Y.; Zhang, X.; Huang, H.; Lifshitz, Y.; Lee, S.-T.; Zhong, J.; Kang, Z. Metal-free efficient photocatalyst for stable visible water splitting via a two-electron pathway. *Science* **2015**, *347*, 970−974. (f) Xiao, X.; Jiang, J.; Zhang, L. Selective oxidation of benzyl alcohol into benzaldehyde over semiconductors under visible light: The case of $Bi_{12}O_{17}Cl_2$ nanobelts. *Appl. Catal., B* **2013**, *142*−*143*, 487−493. (g) Mase, K.; Yoneda, M.; Yamada, Y.; Fukuzumi, S. Efficient Photocatalytic Production of Hydrogen Peroxide from Water and Dioxygen with Bismuth Vanadate and a Cobalt(II) Chlorin Complex. *ACS Energy Lett.* **2016**, *1*, 913−919. (h) Zhang, T.; Schilling, W.; Khan, S. U.; Ching, H. Y. V.; Lu, C.; Chen, J.; Jaworski, A.; Barcaro, G.; Monti, S.; De-Wael, K.; Slabon, A.; Das, S. Atomic Level Understanding for the Enhanced Generation of Hydrogen Peroxide by Aryl Amino Polymeric Carbon Nitrides. *ACS Catal.* **2021**, *11*, 14087−14101.

(12) (a) Ma, R.; Wang, L.; Wang, H.; Liu, Z.; Xing, M.; Zhu, L.; Meng, X.; Xiao, F.-S. Solid acids accelerate the photocatalytic hydrogen peroxide synthesis over a hybrid catalyst of titania nanotube with carbon dot. *Appl. Catal., B* **2019**, *244*, 594−603. (b) Shiraishi, Y.; Kanazawa, S.; Kofuji, Y.; Sakamoto, H.; Ichikawa, S.; Tanaka, S.; Hirai, T. Sunlight-Driven Hydrogen Peroxide Production from Water and Molecular Oxygen by Metal-Free Photocatalysts. *Angew. Chem., Int. Ed.* **2014**, *53*, 13454−13459; *Angew. Chem.* **2014**, *126*, 13672−13677. (c) Kofuji, Y.; Ohkita, S.; Shiraishi, Y.; Sakamoto, H.; Tanaka, S.; Ichikawa, S.; Hirai, T. Graphitic Carbon Nitride Doped with Biphenyl Diimide: Efficient Photocatalyst for Hydrogen Peroxide Production from Water and Molecular Oxygen by Sunlight. *ACS Catal.* **2016**, *6*, 7021−7029. (d) Kofuji, Y.; Ohkita, S.; Shiraishi, Y.; Sakamoto, H.; Ichikawa, S.; Tanaka, S.; Hirai, T. Mellitic Triimide-Doped Carbon Nitride as Sunlight-Driven Photocatalysts for Hydrogen Peroxide Production. *ACS Sustain. Chem. Eng.* **2017**, *5*, 6478−6485. (e) Ou, H.; Yang, P.; Lin, L.; Anpo, M.; Wang, X. Carbon Nitride Aerogels for the Photoredox Conversion of Water. *Angew. Chem., Int. Ed.* **2017**, *56*, 10905−10910; *Angew. Chem.* **2017**, *129*, 11045−11050. (f) Li, S.; Dong, G.; Hailili, R.; Yang, L.; Li, Y.; Wang, F.; Zeng, Y.; Wang, C. Effective photocatalytic H_2O_2 production under visible light irradiation at g-C_3N_4 modulated by carbon vacancies. *Appl. Catal., B* **2016**, *190*, 26−35. (g) Wei, Z.; Liu, M.; Zhang, Z.; Yao, W.; Tan, H.; Zhu, Y. Efficient visible-light-driven selective oxygen reduction to hydrogen peroxide by oxygen-enriched graphitic carbon nitride polymers. *Energy Environ. Sci.* **2018**, *11*, 2581−2589. (h) Samanta, S.; Yadav, R.; Kumar, A.; Kumar Sinha, A.; Srivastava, R. Surface modified C, O co-doped polymeric g-C_3N_4 as an efficient photocatalyst for visible light assisted CO_2 reduction and H_2O_2 production. *Appl. Catal., B* **2019**, *259*, 118054. (i) Kofuji, Y.; Isobe, Y.; Shiraishi, Y.; Sakamoto, H.; Tanaka, S.; Ichikawa, S.; Hirai, T. Carbon Nitride−Aromatic Diimide−Graphene Nanohybrids: Metal-Free Photocatalysts for Solar-to-Hydrogen Peroxide Energy Conversion with 0.2% Efficiency. *J. Am. Chem. Soc.* **2016**, *138*, 10019−10025. (j) Krishnaraj, C.; Sekhar Jena, H.; Bourda, L.; Laemont, A.; Pachfule, P.; Roeser, J.; Chandran, C. V.; Borgmans, S.; Rogge, S. M. J.; Leus, K.; Stevens, C. V.; Martens, J. A.; Van Speybroeck, V.; Breynaert, E.; Thomas, A.; Van Der Voort, P. Strongly Reducing (Diarylamino)benzene-Based Covalent Organic Framework for Metal-Free Visible Light Photocatalytic H_2O_2 Generation. *J. Am. Chem. Soc.* **2020**, *142*, 20107−20116. (k) Fan, W.; Zhang, B.; Wang, X.; Ma, W.; Li, D.; Wang, Z.; Dupuis, M.; Shi, J.; Liao, S.; Li, C. Efficient hydrogen peroxide synthesis by metal-free polyterthiophene via photoelectrocatalytic dioxygen reduction. *Energy Environ. Sci.* **2020**, *13*, 238−245. (l) Teng, Z.; Cai, W.; Liu, S.; Wang,

https://doi.org/10.1021/jacs.1c10786
J. Am. Chem. Soc. XXXX, XXX, XXX−XXX

C.; Zhang, Q.; Chenliang, S.; Ohno, T. Bandgap engineering of polymetric carbon nitride copolymerized by 2,5,8-triamino-tri-s-triazine (melem) and barbituric acid for efficient nonsacrificial photocatalytic H_2O_2 production. *App Catal. B* **2020**, *271*, 118917. (m) Yamada, Y.; Nomura, A.; Miyahigashi, T.; Ohkubo, K.; Fukuzumi, S. Acetate Induced Enhancement of Photocatalytic Hydrogen Peroxide Production from Oxalic Acid and Dioxygen. *J. Phys. Chem. A* **2013**, *117*, 3751−3760.

(13) Hou, W.-C.; Wang, Y.-S. Photocatalytic Generation of H_2O_2 by Graphene Oxide in Organic Electron Donor-Free Condition under Sunlight. *ACS Sustain. Chem. Eng.* **2017**, *5*, 2994−3001.

(14) (a) Zeng, X.; Wang, Z.; Wang, G.; Gengenbach, T. R.; McCarthy, D. T.; Deletic, A.; Yu, J.; Zhang, X. Highly dispersed TiO_2 nanocrystals and WO_3 nanorods on reduced graphene oxide: Z-scheme photocatalysis system for accelerated photocatalytic water disinfection. *Appl. Catal., B* **2017**, *218*, 163−173. (b) Chu, C.; Zhu, Q.; Pan, Z.; Gupta, S.; Huang, D.; Du, Y.; Weon, S.; Wu, Y.; Muhich, C.; Stavitski, E.; Domen, K.; Kim, J.-H. Spatially separating redox centers on 2D carbon nitride with cobalt single atom for photocatalytic H_2O_2 production. *Proc. Natl. Acad. Sci. U.S.A.* **2020**, *117*, 6376−6382. (c) Song, H.; Wei, L.; Chen, C.; Wen, C.; Han, F. Photocatalytic production of H_2O_2 and its in situ utilization over atomic-scale Au modified MoS_2 nanosheets. *J. Catal.* **2019**, *376*, 198−208. (d) Teng, Z.; Zhang, Q.; Yang, H.; Kato, K.; Yang, W.; Lu, Y.-R.; Liu, S.; Wang, C.; Yamakata, A.; Su, C.; Liu, B.; Ohno, T. Atomically dispersed antimony on carbon nitride for the artificial photosynthesis of hydrogen peroxide. *Nat. Catal.* **2021**, *4*, 374−384.

(15) Lu, Y.; Huang, Y.; Zhang, Y.; Huang, T.; Li, H.; Cao, J.; Ho, W. Effects of H_2O_2 generation over visible light-responsive Bi/$Bi_2O_{2-x}CO_3$ nanosheets on their photocatalytic NO_x removal performance. *Chem. Eng. J.* **2019**, *363*, 374−382.

(16) (a) Chen, X.; Kondo, Y.; Kuwahara, Y.; Mori, K.; Louis, C.; Yamashita, H. Metal−organic framework-based nanomaterials for photocatalytic hydrogen peroxide production. *Phys. Chem. Chem. Phys.* **2020**, *22*, 14404−14414. (b) Kawase, Y.; Isaka, Y.; Kuwahara, Y.; Mori, K.; Yamashita, H. Ti cluster-alkylated hydrophobic MOFs for photocatalytic production of hydrogen peroxide in two-phase systems. *Chem. Commun.* **2019**, *55*, 6743−6746.

(17) Hou, H.; Zeng, X.; Zhang, X. Production of Hydrogen Peroxide by Photocatalytic Processes. *Angew. Chem., Int. Ed.* **2020**, *59*, 17356−17376.

(18) Wu, Q.; Cao, J.; Wang, X.; Liu, Y.; Zhao, Y.; Wang, H.; Liu, Y.; Huang, H.; Liao, F.; Shao, M.; Kang, Z. A metal-free photocatalyst for highly efficient hydrogen peroxide photoproduction in real seawater. *Nat. Commun.* **2021**, *12*, 483.

(19) Mase, K.; Yoneda, M.; Yamada, Y.; Fukuzumi, S. Seawater usable for production and consumption of hydrogen peroxide as a solar fuel. *Nat. Commun.* **2016**, *7*, 11470.

(20) Baek, J. H.; Gill, T. M.; Abroshan, H.; Park, S.; Shi, X.; Nørskov, J.; Jung, H. S.; Siahrostami, S.; Zheng, X. Selective and Efficient Gd-Doped $BiVO_4$ Photoanode for Two-Electron Water Oxidation to H_2O_2. *ACS Energy Lett.* **2019**, *4*, 720−728.

(21) Zhang, K.; Liu, J.; Wang, L.; Jin, B.; Yang, X.; Zhang, S.; Park, J. H. Near-Complete Suppression of Oxygen Evolution for Photoelectrochemical H_2O Oxidative H_2O_2 Synthesis. *J. Am. Chem. Soc.* **2020**, *142*, 8641−8648.

(22) United Nations Department of Economic and Social Affairs. The 17 Goals − Sustainable Development, https://sdgs.un.org/goals (accessed 2021-09-14).

(23) Shan, R.; Lu, L.; Shi, Y.; Shi, J. Catalysts from renewable resources for biodiesel production. *Energy Convers. Manag.* **2018**, *178*, 277−289.

(24) Zhu, Y.; Li, Z.; Chen, J. Applications of lignin-derived catalysts for green synthesis. *Green Energy Environ.* **2019**, *4*, 210−244.

(25) Budnyak, T. M.; Onwumere, J.; Pylypchuk, I. V.; Jaworski, A.; Chen, J.; Rokicińska, A.; Lindström, M. E.; Kuśtrowski, P.; Sevastyanova, O.; Slabon, A. LignoPhot: Conversion of hydrolysis lignin into the photoactive hybrid lignin/$Bi_4O_5Br_2$/BiOBr composite for simultaneous dyes oxidation and Co^{2+} and Ni^{2+} recycling. *Chemosphere* **2021**, *279*, 130538.

(26) Landaeta, E.; Schultz, Z. D.; Burgos, A.; Schrebler, R.; Isaacs, M. Enhanced photostability of cuprous oxide by lignin films on glassy carbon electrodes in the transformation of carbon dioxide. *Green Chem.* **2018**, *20*, 2356−2364.

(27) Khan, A.; Nair, V.; Colmenares, J. C.; Gläser, R. Lignin-Based Composite Materials for Photocatalysis and Photovoltaics. *Top Curr. Chem.* **2018**, *376* (3), 20.

(28) Budnyak, T. M.; Slabon, A.; Sipponen, M. H. Lignin−Inorganic Interfaces: Chemistry and Applications from Adsorbents toCatalysts and Energy Storage Materials. *ChemSusChem.* **2020**, *13*, 4344−4355.

(29) (a) Kageyama, H.; Hayashi, K.; Maeda, K.; Attfield, P. J.; Hiroi, Z.; Rondinelli, J. M.; Poeppelmeier, K. R. Expanding frontiers in materials chemistry and physics with multiple anions. *Nat. Commun.* **2018**, *9*, 772. (b) Guo, M.; Zhou, Z.; Yan, S.; Zhou, P.; Miao, F.; Liang, S.; Wang, J.; Cui, X. Bi_2WO_6−BiOCl heterostructure with enhanced photocatalytic activity for efficient degradation of oxytetracycline. *Sci. Rep.* **2020**, *10*, 18401. (c) Zhang, X.; Ai, Z.; Jia, F.; Zhang, L. Generalized One-Pot Synthesis, Characterization, and Photocatalytic Activity of Hierarchical BiOX (X = Cl, Br, I) Nanoplate Microspheres. *J. Phys. Chem. C* **2008**, *112*, 747−753. (d) Li, H.; Shang, J.; Ai, Z.; Zhang, L. Efficient Visible Light Nitrogen Fixation with BiOBr Nanosheets of Oxygen Vacancies on the Exposed {001} Facets. *J. Am. Chem. Soc.* **2015**, *137*, 6393−6399. (e) Cheng, H.; Huang, B.; Dai, Y. Engineering BiO_X (X = Cl, Br, I) nanostructures for highly efficient photocatalytic applications. *Nanoscale* **2014**, *6*, 2009−2026.

(30) Zhu, C.; Liu, C.; Fu, Y.; Gao, J.; Huang, H.; Liu, Y.; Kang, Z. Construction of CDs/CdS photocatalysts for stable and efficient hydrogen production in water and seawater. *Appl. Catal., B* **2019**, *242*, 178−185.

(31) Yang, Y.; Liu, L.; Qi, Q.; Chen, F.; Qiu, M.; Gao, F.; Chen, J. A low-cost and stable Fe_2O_3/C-TiO_2 system design for highly efficient photocatalytic H_2 production from seawater. *Catal. Commun.* **2020**, *143*, 106047.

(32) Liu, Y.; Liao, Z.; Ma, X.; Xiang, Z. Ultrastable and Efficient Visible-Light-Driven Hydrogen Production Based on Donor−Acceptor Copolymerized Covalent Organic Polymer. *ACS Appl. Mater. Interfaces* **2018**, *10*, 30698−30705.

(33) Fujii, M.; Rose, A. L.; Waite, T. D.; Omura, T. Oxygen and Superoxide-Mediated Redox Kinetics of Iron Complexed by Humic Substances in Coastal Seawater. *Environ. Sci. Technol.* **2010**, *44*, 9337−9342.

(34) Capanema, E. A.; Balakshin, M. Y.; Kadla, J. F. A Comprehensive Approach for Quantitative Lignin Characterization by NMR Spectroscopy. *J. Agric. Food Chem.* **2004**, *52*, 1850−1860.

(35) Sillen, L. X-ray studies on BiOCl, BiOBr and BiOI. *Svensk Kemisk Tidskrift* **1941**, *53*, 39−43.

(36) Xu, J.; Mao, Y.-G.; Liu, T.; Peng, Y. Synthesis of a novel one-dimensional BiOBr−$Bi_4O_5Br_2$ heterostructure with a high quality interface and its enhanced visible-light photocatalytic activity. *CrystEngComm* **2018**, *20*, 2292−2298.

(37) Divya, J.; Shivaramu, N. J.; Purcell, W.; Roos, W. D.; Swart, H. C. Effects of annealing temperature on the crystal structure, optical and photocatalytic properties of Bi_2O_3 needles. *Appl. Surf. Sci.* **2020**, *520*, 146294.

(38) Onwumere, J.; Piątek, J.; Budnyak, T.; Chen, J.; Budnyk, S.; Karim, Z.; Thersleff, T.; Kuśtrowski, P.; Mathew, A. P.; Slabon, A. CelluPhot: Hybrid Cellulose-Bismuth Oxybromide Membrane for Pollutant Removal. *ACS Appl. Mater. Interfaces* **2020**, *12*, 42891−42901.

(39) Li, R.; Xie, F.; Liu, J.; Wang, Y.; Wang, Y.; Zhang, X.; Fan, C. Synthesis of $Bi_4O_5Br_2$ from reorganization of BiOBr and its excellent visible light photocatalytic activity. *Dalton Trans.* **2016**, *45*, 9182−9186.

https://doi.org/10.1021/jacs.1c10786
J. Am. Chem. Soc. XXXX, XXX, XXX−XXX